

# Noncollisional heating and electron energy distributions in magnetically enhanced inductively coupled and helicon plasma sources

Ronald L. Kinder<sup>a)</sup> and Mark J. Kushner<sup>b)</sup>

*Department of Electrical and Computer Engineering, University of Illinois, 1406 West Green Street, Urbana, Illinois 61801*

(Received 5 April 2001; accepted for publication 13 July 2001)

The ability to deposit power in the volume of plasma reactors at locations deeper than the conventional skin depth makes magnetically enhanced inductively coupled plasma (MEICP) and helicon sources appealing for use in materials processing. Mechanisms for power deposition and electron energy transport in MEICPs have been computationally investigated using a two-dimensional (2D) plasma equipment model. Using a tensor conductivity in the solution of Maxwell's equations, three-dimensional components of the inductively coupled electric field are produced from an  $m=0$  antenna and 2D applied magnetic fields. These fields are then used in a Monte Carlo simulation to generate electron energy distributions (EEDs), transport coefficients, and electron impact source functions. The electrostatic component of the wave is resolved by estimating the charge density using an oscillatory perturbed electron density. For MEICPs operating at pressures less than 10 mTorr in Ar, significant power deposition occurs downstream when the radial and axial components of the electric field are commensurate with the azimuthal component. For magnetic fields above 100 G, the tail of the EED ( $>20$ – $30$  eV) is enhanced in the downstream region. This enhancement results from noncollisional heating by the axial electric field for electrons in the tail of the EED which have long mean free paths, while lower energy electrons are still somewhat collisional. © 2001 American Institute of Physics. [DOI: 10.1063/1.1400091]

## I. INTRODUCTION

Magnetically enhanced inductively coupled plasma (MEICP) and helicon plasma sources are being developed for their high ionization efficiency and their ability to deposit power within the volume of the plasma.<sup>1–7</sup> These sources typically have a higher plasma density for a given power deposition than conventional ICP sources.<sup>8–11</sup> The mechanisms through which more efficient heating of electrons occurs in these systems are not well understood. One common characteristic of many MEICP and helicon devices is their ability to produce a maximum in the plasma density in the downstream region of processing chambers (remote from the antenna), which implies that substantial power deposition also occurs downstream.<sup>12,13</sup>

Carter and Khachan experimentally investigated an  $m=0$  helicon source sustained in argon. They showed that the electric fields in the downstream region are a superposition of higher order radial modes and their reflections from the endplate.<sup>14</sup> The on axis ion density, measured with Langmuir probes, generally increased with increasing distance from the antenna. For a constant power deposition, the highest ion density was obtained at low magnetic fields ( $\sim 15$  G) where the phase velocity of the electromagnetic wave was commensurate with the thermal speed of electrons. They also found that the ion density, peaking on axis at low magnetic fields, had off axis peaks at high magnetic fields. Borg and

Kamenski, showed that, for low magnetic field plasma sources, the response of the electron energy distribution (EED) near the antenna indicated a strong a wave–electron interaction.<sup>15</sup> They proposed that, for helicon wave driven plasma sources, the dominant collisionless wave–particle interaction mechanism is electron acceleration by the parallel component of the electric field. The heating of electrons by wave damping is dominant in the far field.

Landau damping has been proposed as a mechanism through which more efficient heating may occur.<sup>16</sup> In this process, energetic primary electrons are produced through trapping and acceleration by a helicon wave. The electrons produce ionizations, lowering their energy and generating a low energy secondary. The wave reaccelerates electrons after each ionization event. Gui and Scharer performed simulations of electron trajectories in an  $m=+1$  helicon plasma source sustained in argon. They found that trapped electrons appeared as the magnetic field amplitude increased. The EED displayed a bunching of particles with energies higher than the ionization potential of the gas.<sup>17</sup> Recent measurements of the phase of the optical emission from high lying short lived excited states of  $\text{Ar}^+$  in an  $m=+1$  helicon source showed that the emission correlated well with the phase velocity of the helicon wave.<sup>18</sup> Simulations by Deggeling and Boswell demonstrated that maxima in the ionization rate in an argon plasma traveled away from the antenna at the phase velocity of the wave. This implies that resonant electrons are trapped in the wave reference frame.<sup>19</sup> It was found that the ionization rate was highest when the phase velocity of the wave was  $2$ – $3 \times 10^8$  cm s<sup>-1</sup>. This value is commensurate with the thermal speed of electrons which

<sup>a)</sup>Present address: Novellus Systems, 4000 North First St., San Jose, CA 95134; electronic mail: ron.kinder@novellus.com

<sup>b)</sup>Author to whom correspondence should be addressed; electronic mail: mjk@uiuc.edu

have energies just above the ionization threshold. These observations support the proposal that electron trapping in the axial electric field is the underlying mechanism that drives high density, collisionlessly heated plasmas.

Additional support comes from measurements by Molvik *et al.* who, using an electron energy analyzer, demonstrated that electrons having energies above the plasma potential are correlated with the rf phase.<sup>20</sup> Their results showed that transit-time heating of electrons is sufficient to account for enhancements of the tail of the EED. They observed energy deposition downstream of the antenna if the phase velocity of the axial wave is in the range corresponding to electron energies of about 25 eV. Collisions have a strong effect on reducing the wave-particle phase coherence and so these effects should be less pronounced at higher pressures.

In more recent work, Chen and Blackwell found that there may, in fact, be too few phased fast electrons to account for the majority of ionization to occur through Landau damping.<sup>21</sup> However, they could not rule out heating by nonlinear processes under and near the antenna at low electron densities, as advocated by Ellingboe and co-workers.<sup>22,23</sup> Indeed, fast electrons oscillating in standing waves under the antenna or injected into the plasma just past the antenna are subjected to beam-plasma instabilities and could thermalize rapidly. More recently, Kwak suggested that much of the electron heating comes from an electrostatic component of the helicon wave.<sup>24</sup>

When a finite electron mass is taken into account in a cold plasma model another solution to the wave equation appears in bounded geometries at frequencies above the lower hybrid. This is referred to as the electrostatic Trivelpiece-Gould (TG) mode and was identified by Trivelpiece and Gould as the cavity eigenmode of a cold plasma, space charge wave in a cylinder.<sup>25</sup> Being nearly electrostatic and of short radial wavelength, these waves are strongly absorbed as they propagate perpendicular to the externally applied static magnetic field lines. Damping of the TG mode has also been proposed for power deposition in helicon sources.<sup>26</sup> In this regard, it has been suggested that helicon waves deposit power by coupling to TG waves at the radial boundary. Strongly damped electrostatic waves can reach the plasma core at low magnetic fields, while at high fields they deposit power at the periphery of the plasma column. Power deposition in the volume of plasmas occurs at high magnetic fields in special antiresonance regimes when the excitation of the electrostatic wave is suppressed.<sup>27</sup> There is still discussion as to the influence of these mechanisms on electron heating. Borg and Boswell have suggested that for conditions where the rf frequency is near the lower hybrid frequency, the TG mode does not lead to a significant increase in antenna coupling in a helicon plasma.<sup>28</sup> However, the TG mode may enhance wave damping due to its high amplitude electric field in the presence of high electron collision rates.

In industrial plasma sources where magnetic fields typically span a large range of values and modes are likely not to be pure, power deposition likely has contributions from both mechanisms. For example, Mouzouris and Scharer proposed that the TG mode may dominate electron heating at low

magnetic fields where power is deposited near the edge region.<sup>29</sup> At higher magnetic fields ( $>80$  G), the propagating helicon mode then deposits power in the core of the plasma away from the antenna. Collisional damping may be the dominant heating mechanism at moderate pressures ( $>2$  mTorr) and higher densities ( $\geq 2 \times 10^{12}$  cm<sup>-3</sup>). However, at lower pressures ( $<2$  mTorr) Landau damping may be an important heating mechanism, provided that resonant electrons have velocities near that of the wave phase velocity. Landau damping may also occur over a broad range of energies (10–100 eV), in contrast to earlier predictions of narrow energetic beams.<sup>30</sup>

To investigate the coupling of electromagnetic waves to the plasma in MEICPs and their effects on EEDs algorithms were developed for wave propagation in the presence of static magnetic fields using the two-dimensional Hybrid Plasma Equipment Model (HPEM).<sup>31–33</sup> A full tensor conductivity was added to the Electromagnetics Module which enables one to calculate three-dimensional components of the inductively coupled electric field based on two-dimensional applied magnetostatic fields. Electromagnetic fields were obtained by solving the three-dimensional (3D) wave equation. These 3D fields were used in the Electron Monte Carlo Simulation (EMCS) of the HPEM to obtain EEDs as a function of position.

This study was divided into two parts. In the first part, plasma neutrality was enforced in the solution of Maxwell's equations so the effects of the TG mode on plasma heating were ignored. This separation of the two heating mechanism components is valid for the  $m=0$  analysis performed here. Unlike higher order modes, such as the  $m=\pm 1$ , where a 3D coil design can generate significant electrostatic fields, it is possible to suppress the TG mode in an  $m=0$  design. The purpose of this part of the investigation was to determine the effects of helicon waves on the EED and on the ability to deposit power downstream of the antenna. We found that, in the absence of the TG mode, with increasing magnetic field electric field propagation progressively follows magnetic field lines and significant power can indeed be deposited downstream. The tails of the EEDs are enhanced in the downstream region, indicating some amount of electron trapping and collisionless acceleration by the axial electric field for electrons having long mean free paths. These collisionless electrons typically reside in the tail of the EED while low energy electrons in the bulk of the EED are more collisional.

The second part of the study focused on resolving the TG mode by including the divergence term in the solution of the wave equation. The electrostatic term was approximated by a harmonically driven perturbation of the electron density. The results indicate that the effect of the TG mode is to restructure power deposition near the coils. However, the propagation of the helicon component is little affected, particularly at large magnetic fields where the TG mode is damped. For  $m=0$  excitation, the TG mode does not significantly contribute as a heating mechanism.

Plasma parameters, wave propagation, and power deposition efficiency are discussed for Ar gas as a function of magnetic field strength, configuration, and power. The model

will be described in Sec. II, followed by a discussion of our results for EEDs when excluding the electrostatic component of the wave in Sec. III. The effects of the TG mode on heating and EEDs are discussed in Sec. IV. Concluding remarks are in Sec. V.

## II. DESCRIPTION OF THE MODEL

The two-dimensional (2D) HPEM was improved to address issues concerning heating mechanisms and wave propagation in MEICPs. The hybrid model and the improved electromagnetics module used in this work are described in detail elsewhere<sup>31–33</sup> and will only briefly be discussed here. The HPEM is a two-dimensional, plasma equipment simulator which consists of the Electromagnetic Module (EMM), the Electron Energy Transport Module (EETM), and the Fluid Kinetics Module (FKM). Electromagnetic fields and corresponding phases are calculated in the EMM. These fields are then used in the EETM to obtain electron impact source functions and transport coefficients. This can be accomplished by solving the electron energy equation or by using the EMCS. These parameters are transferred to the FKM where momentum, continuity and energy equations are solved for all heavy particles. A drift diffusion formulation is used for electrons to enable an implicit solution of Poisson's equation for the electric potential. The species densities and electrostatic fields produced in the FKM are transferred to the EMCS and the EMM. These modules are iterated until a converged solution is obtained.

The EMM portion of the plasma model was improved to resolve three-dimensional components of the inductively coupled electric field based on two-dimensional applied magnetostatic fields and azimuthal antenna currents, previously described in Ref. 33. The results discussed here are for a two-dimensional ( $r, z$ ) azimuthally symmetric geometry. Given azimuthal antenna currents and ( $r, z$ ) magnetostatic fields, all three components of the inductively coupled electric field ( $r, \theta, z$ ) are generated, and we therefore solve for these three components. Previously, plasma neutrality was enforced when solving the wave equation. However in order to resolve the TG mode, the electrostatic term in the wave equation must be taken into account. The electromagnetic fields,  $\bar{E}$ , are then obtained by solving the following form of the wave equation:

$$\nabla \cdot \left( \frac{1}{\mu} \nabla \cdot \bar{E} \right) - \nabla \cdot \left( \frac{1}{\mu} \nabla \bar{E} \right) - \omega^2 \epsilon \bar{E} = -i\omega(\bar{J} + \bar{\sigma} \cdot \bar{E}), \quad (1)$$

where  $\bar{J}$ ,  $\omega$ ,  $\epsilon$ ,  $\mu$ , and  $\bar{\sigma}$  are the external antenna current density, angular electromagnetic frequency, permittivity, permeability and tensor conductivity, respectively. The ion current in solution of Eq. (1) is ignored due to the low mobility of ions. The conduction current is addressed by a warm plasma tensor described in Ref. 33. An analogous full tensor mobility is used for electron transport in the electron energy equation option of the EETM and in the FKM. Equation (1) is solved for the electromagnetic fields using a sparse matrix conjugate gradient method.<sup>34</sup>

The leading divergence term in Eq. (1) is included by using a perturbation form of Poisson's equation. For a

quasineutral plasma, neglecting ion mobility over the rf cycle, the divergence of the electric field is equal to the perturbation in the electron density from neutrality, defined as,

$$\nabla \cdot \bar{E} = \frac{\rho}{\epsilon} = \frac{\sum_i q n_i}{\epsilon} = \frac{q N_+ + q N_- + q n_e + q \Delta n_e}{\epsilon} = \frac{q \Delta n_e}{\epsilon}, \quad (2)$$

where  $\rho$ ,  $n_i$ ,  $N_+$ ,  $N_-$ ,  $n_e$  and  $\Delta n_e$  are the charge density, density of the  $i$ th charge species, total positive ion density, total negative ion density, unperturbed electron density and perturbation to the electron density, respectively. On the time scale of the electromagnetic period, the total electron density,  $n_e(t)$ , is the sum of the steady state electron density,  $n_e$ , and the perturbed electron density,  $\Delta n_e \exp(i\omega t)$ ,

$$\frac{\partial n_e(t)}{\partial t} = \frac{\partial}{\partial t} [n_e + \Delta n_e \exp(i\omega t)] = i\omega \Delta n_e \exp(i\omega t). \quad (3)$$

The magnitude of the perturbed electron density is obtained by solving the continuity equation for the electron density, with an appropriate damping term,

$$\frac{\partial n_e(t)}{\partial t} = -\nabla \cdot (n_e \bar{v}) - \frac{\Delta n_e}{\tau}, \quad (4)$$

$$i\omega \Delta n_e = -\nabla \cdot \left( \frac{\bar{\sigma} \cdot \bar{E}}{q} \right) - \frac{\Delta n_e}{\tau}, \quad (5)$$

$$\Delta n_e = \frac{-\nabla \cdot \left( \frac{\bar{\sigma} \cdot \bar{E}}{q} \right)}{\left( \frac{1}{\tau} + i\omega \right)}, \quad (6)$$

where  $\bar{v}$  and  $\tau$  are the electron velocity and damping factor, respectively. The damping factor takes into account the average time it takes a perturbed electron to return to the steady state. The propagation of the electrostatic wave perpendicular to the static magnetic field lines is limited by a factor proportional to the cyclotron frequency and the plasma frequency.

Electron transport properties and EEDs are obtained from the EMCS. The EMCS integrates electron trajectories from electric and magnetic fields obtained using the EMM and FKM, and employs Monte Carlo techniques for collisions. The electrons are initially given a Maxwellian EED and placed in the reactor using a distribution weighted by the local electron density obtained from the FKM. Pseudoparticle trajectories are advanced using the Lorentz equation,

$$\frac{d\bar{v}}{dt} = \frac{q_e}{m_e} (\bar{E} + \bar{v} \times \bar{B}), \quad (7)$$

and

$$\frac{d\bar{r}}{dt} = \bar{v}, \quad (8)$$

where  $\bar{v}$ ,  $\bar{E}$ , and  $\bar{B}$  are the electron velocity, local electric field and magnetic field, respectively. Equations (7) and (8) are updated using an implicit integration technique which enables a single time step to span a large fraction of the cyclotron period.<sup>35</sup>

The range of electron energies of interest is divided into discrete energy bins. Energy bins have constant widths over a specified energy range to simplify gathering statistical data while resolving the structure in electron impact cross sections. Typically 300–500 total bins are used with energy ranges (100 bins/range depending on the chemistry) of 0–5, 5–15, 15–50, and 50–200 eV. Within energy bin  $i$ , the total collision frequency,  $\nu_i$ , is computed by summing all the possible collisions,

$$\nu_i = \left( \frac{2\epsilon_i}{m_e} \right)^{1/2} \sum_{j,k} \sigma_{ijk} N_j, \quad (9)$$

where  $\epsilon_i$  is the average energy within the bin,  $\sigma_{ijk}$  is the cross section at energy  $i$  for species  $j$  and collision process  $k$ , and  $N_j$  is the number density of species  $j$ . Null collision cross sections are employed for each energy range to provide a constant collision frequency. The integration time step for an electron in a given energy range is then the minimum of the randomly chosen free flight time,  $\tau = -[\ln(r)/\nu_i]$ , the time required to cross a specified fraction of the local computational cell, a specified fraction of the rf period and a specified fraction of the local cyclotron period. Here,  $r$  is a random number distributed on (0,1). Pseudoparticles are allowed to diverge in time until they reach a specified future time. When a pseudoparticle reaches that time, it is no longer advanced until all other particles catch up. After the free-flight time, the type of collision is determined by the choice of a random number. Should the selected collision be null, the pseudoparticle proceeds unhindered. For a real collision, additional random numbers are chosen to determine the type of collision that occurs (and hence the electron energy loss) and the scattering angles. The final velocity is then determined by applying the scattering matrix,

$$\begin{aligned} V_x &= V(\cos \beta \cos \alpha \sin \theta \cos \phi + \cos \beta \sin \alpha \cos \theta \\ &\quad - \sin \beta \sin \theta \sin \phi), \\ V_y &= V(\sin \beta \cos \alpha \sin \theta \cos \phi + \sin \beta \sin \alpha \cos \theta \\ &\quad + \cos \beta \sin \theta \sin \phi), \\ V_z &= V(-\sin \alpha \sin \theta \cos \phi + \cos \alpha \cos \theta), \end{aligned} \quad (10)$$

where  $\alpha$  and  $\beta$  are the polar and azimuthal Eulerian angles prior to the collision;  $\theta$  and  $\phi$  are the polar and azimuthal scattering angles, and  $V$  is the electron speed after the collision. Assuming azimuthal symmetry for the collision,  $\phi$  is randomly chosen from the interval  $(0, 2\pi)$ . Unless experimental data are available,  $\theta$  is chosen by specifying a scattering parameter  $\gamma$  where the polar scattering probability is given by  $\cos^2(\theta/2)$ .  $\gamma=0$  provides for isotropic scattering and  $\gamma \gg 1$  provides for forward scattering. The randomly selected scattering angle is then

$$\theta = 2[\cos^{-1}(1-r)]^{1/(2+\gamma)}, \quad (11)$$

where  $r$  is a random number distributed (0, 1).

Statistics are collected for every particle on every time step. The particles are binned by energy and location with weighting proportional to the product of the number of electrons each pseudoparticle represents and its last time step.

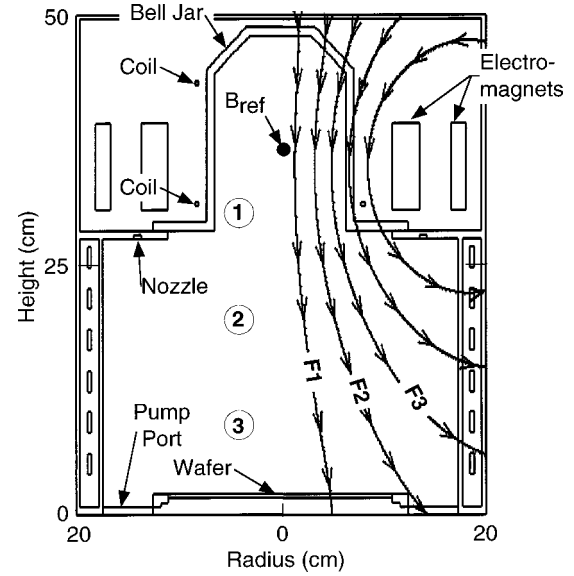


FIG. 1. Model geometry based on the Trikon PMT MORI helicon source. The base case process conditions are Ar, 10 mTorr and 1 kW power deposition. The rf coils are operated 180° out of phase at 13.56 MHz.

Particle trajectories are integrated for  $\approx 100$  rf cycles for each call of the EETM. Statistics are typically gathered for only the latter two thirds of those cycles to allow transients which occur at the beginning of each iteration to damp out.

At the end of a given iteration, the EED at each spatial location is obtained by normalizing the statistics such that

$$\sum_i F_i(\bar{r}) = \sum_i f_i(\bar{r}) \epsilon_i^{1/2} \Delta \epsilon_i = 1, \quad (12)$$

where  $F_i(\bar{r})$  is the sum of the pseudoparticles' weightings at  $\bar{r}$  for energy bin  $i$  having energy  $\epsilon_i$ ,  $f_i(\bar{r})$  ( $\text{eV}^{-3/2}$ ) is the EED at  $\bar{r}$ , and  $\Delta \epsilon_i$  is the width of the energy bin. Electron impact rate coefficients for process  $j$  at location  $\bar{r}$  are determined by convolving the EED with the process cross section,

$$k_j(\bar{r}) = \sum_j f_j(\bar{r}) \epsilon_j^{1/2} \left( \frac{2\epsilon_j}{m_e} \right)^{1/2} \sigma_j(\epsilon_j) \Delta \epsilon_j, \quad (13)$$

where  $\sigma_j$  is the energy dependent cross section for process  $j$ . Source functions for electron impact processes (or, more properly, collision frequency per atom or molecule) are then generated for the current iteration,  $l$ , of the HPFM by

$$S_j^l(\bar{r}) = k_j(\bar{r}) n_e^{l-1}(\bar{r}), \quad (14)$$

where  $n_e^{l-1}(\bar{r})$  is the electron density obtained from the FKM in the previous iteration. The source functions which are actually transferred to the FKM,  $S_{jo}^l$ , may be backaveraged over previous iterations,

$$S_{jo}^l = (1 - \alpha) S_{jo}^l + \alpha S_{jo}^{l-1}, \quad (15)$$

followed by  $S_j^l = S_{jo}^l$ , where  $\alpha$  is a backaveraging coefficient. Typically  $\alpha \approx 0.3-0.5$ .

### III. NONLOCAL HEATING OF EEDs

The geometry used in this investigation is based on the Trikon Technologies, Inc., Pinnacle 8000 helicon plasma

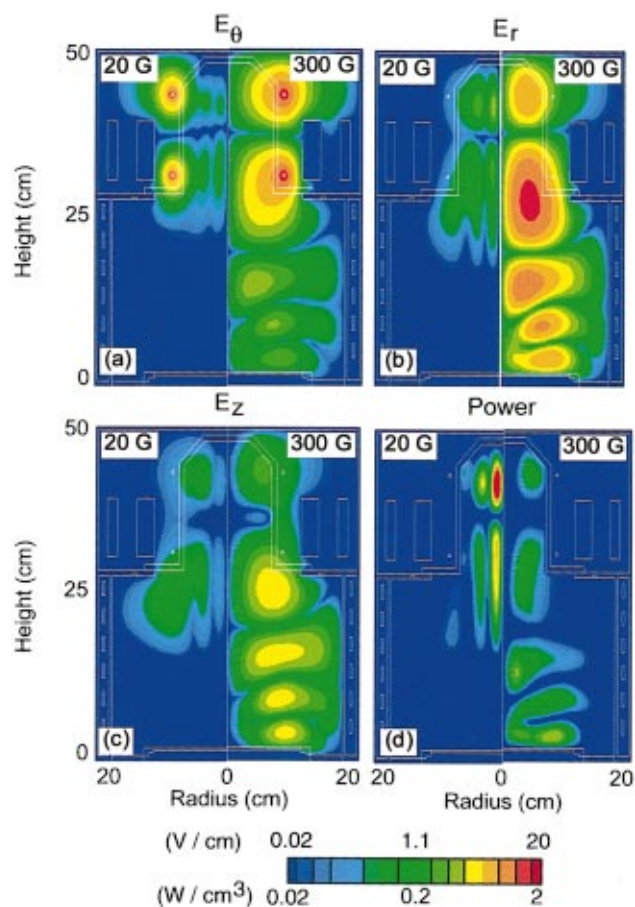


FIG. 2. (Color) Electric field amplitudes and power deposition for static magnetic fields of 20 and 300 G. (a) Azimuthal electric field, (b) radial electric field, (c) axial electric field, (d) power deposition. The process conditions are Ar, 10 mTorr and 1 kW. An increase in magnetic field produces radial and axial components of the electric field and propagation in the axial direction.

source, schematically shown in Fig. 1. A quartz bell jar is surrounded by electromagnets which produce a solenoidal magnetic field which flares in the downstream chamber, as shown on the right side of Fig. 1. The magnetic field magnitudes cited in the following discussion are for an on axis location midway between the antennas, denoted as  $B_{\text{ref}}$  in Fig. 1. The system is powered by two ring coils surrounding the bell jar. Each coil operates at 13.56 MHz and is  $180^\circ$  out of phase with each other. Processing gas is injected through a nozzle located below the electromagnets and is exhausted through a pump port surrounding the outside diameter of the grounded substrate. The base case operating conditions are Ar gas at 10 mTorr and 50 sccm, and a power deposition of 1 kW. The reaction mechanism used for Ar is discussed in Ref. 36. Electron-ion scattering is included in the Monte Carlo simulation although electron-electron scattering is not. Throughout this article, EEDs will be shown for three axial locations along the flux lines labeled, F1, F2, and F3 as shown on the right side of Fig. 1. The axial positions are labeled 1 ( $z=27$  cm), 2 ( $z=18$  cm) and 3 ( $z=9$  cm) on the left side of Fig. 1. Assuming that electrons are magnetized in fields greater than tens of G, sampling electrons along a flux line tracks approximately the same population of electrons.

Azimuthal, radial and axial electric field amplitudes and power deposition for the base case are shown in Fig. 2 for magnetic fields of 20 and 300 G. For these results, transport coefficients were obtained using the EMCS while neglecting the electrostatic term in Maxwell's equation. Propagation of electromagnetic fields and power deposition in this geometry are discussed elsewhere<sup>33</sup> and so only a brief description will be provided here. At  $B=20$  G, the azimuthal electric field is predominantly inductively coupled with an enhanced plasma skin depth, as shown in the left half of Fig. 2(a). Radial and axial electric fields are generated by the tensor conductivity and indicate the onset of a radially traveling wave, shown on the left side of Figs. 2(b) and 2(c). The skin depth has increased beyond the axis of symmetry and a standing wave pattern begins to develop. As the magnetic field is increased to 300 G, further penetration of the electromagnetic fields into the plasma occurs, as shown on the right side of Fig. 2. As the radial penetration increases, the relative axial conductivity also increases, thereby allowing the electromagnetic fields to propagate downstream. When the propagating wave encounters a boundary, such as the substrate, a standing wave pattern forms, here in the axial direction. The profiles for power deposition reflect those of the electromagnetic fields. At 300 G, significant power is deposited downstream, as shown in Fig. 2(d). At 20 G, the power deposition peaks at  $2.1 \text{ W/cm}^3$ . At 300 G the same total power is deposited over a larger volume, resulting in a lower peak power deposition of  $1.1 \text{ W/cm}^3$ .

The electron temperature (defined by  $\frac{2}{3}\langle\epsilon\rangle$ ), derived from the EMCS, and the electron density are shown in Fig. 3. At 20 G the electron temperature peaks in the bell jar at  $\approx 4$  eV where most of the power deposition occurs. However, at 300 G the electron temperature peaks downstream, as shown on the right side of Fig. 3(a), at about 3.6 eV. As will be discussed below, the axial component of the electric field is responsible for heating the electrons downstream. As electrons are accelerated by the axially propagating wave, they can absorb substantial power from the field in spite of the plasma being somewhat collisional. At 10 mTorr, the electron density is a maximum near the location of peak power deposition, as shown in Fig. 3(b). At 20 G, the peak plasma density occurs in the bell jar at  $\approx 4 \times 10^{12} \text{ cm}^{-3}$ . At 300 G, the downstream power deposition allows for a large plasma density in the lower chamber, peaking at about  $3.2 \times 10^{12} \text{ cm}^{-3}$ .

The EED along the magnetic flux lines at the reference axial positions are shown in Fig. 4 for a magnetic field of 20 G. The EEDs along the magnetic field line F1, shown in Fig. 4(a), are closely spaced, indicating that the electron temperature remains fairly constant. The EEDs along F2 show a small increase in the high energy tail of the distribution at positions progressively further away from the coil. The increase is not substantial enough to conclude that there is significant axial heating downstream. The EEDs along F3 are similar for positions 1 ( $z=27$  cm) and 2 ( $z=18$  cm). However, the EED at position 3 ( $z=9$  cm) has a lower high energy tail. The field line F3 is significantly divergent and so electrons have physically traversed more gas to reach a location that is fairly close to the chamber wall for position 3.

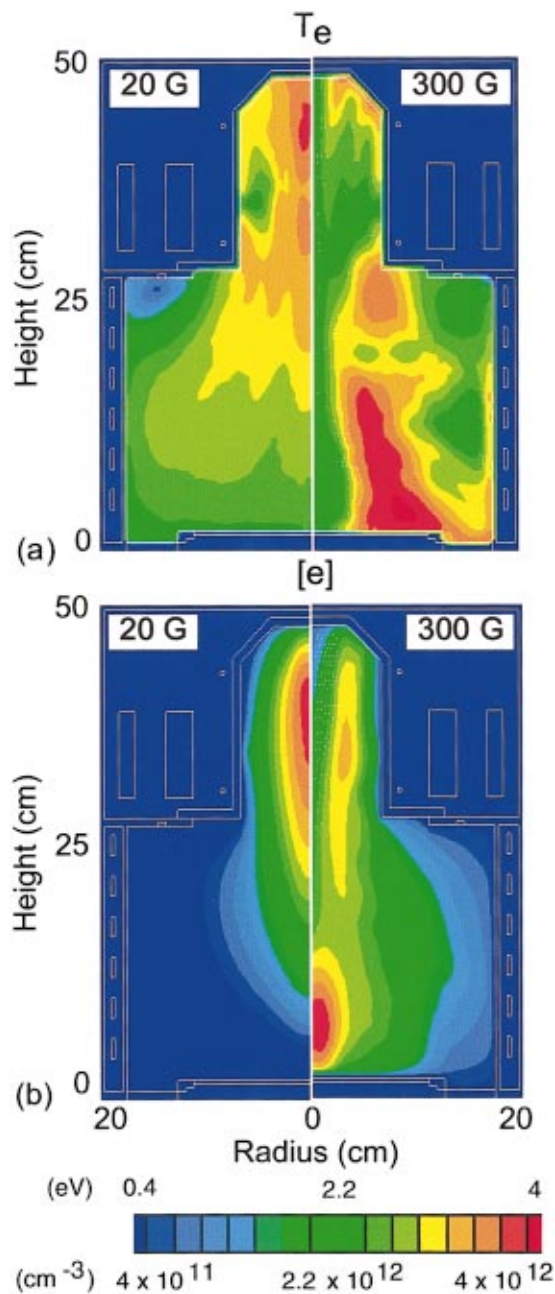


FIG. 3. (Color) Plasma properties for static magnetic fields of 20 and 300. (a) Electron temperature and (b) electron density. The process conditions are Ar, 10 mTorr and 1 kW power deposition. An increase in magnetic field enables peak temperatures and electron densities downstream.

Electrons reaching this point, having traversed a larger column density of gas into a region of lower electric field, have a colder EED.

The EEDs for a magnetic field of 300 G are shown in Fig. 5. Along F1, the EEDs at the three axial locations overlap, with a small increase in the high energy tail for position 3 ( $z=9$  cm), as shown in Fig. 5(a). Electrons on F1 are close to the line of symmetry where electric fields are small (or zero) and so on the average are cooler. At the higher magnetic field, electrons on F1 have sufficiently low transverse mobility that they do not sample the larger electric fields at larger radii. However, along F2, there is a substantial increase in the high energy tail of the EED at positions pro-

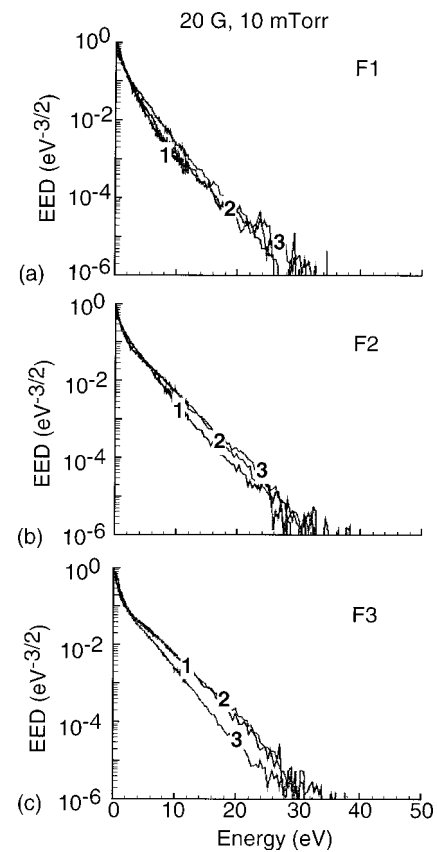


FIG. 4. EEDs along the magnetic flux lines: (a) F1, (b) F2, and (c) F3. EEDs are shown for reference axial positions 1 ( $z=27$  cm), 2 ( $z=18$  cm) and 3 ( $z=9$  cm) for 20 G and 10 mTorr.

gressively further from the coil, as shown in Fig. 5(b). This raising of the tail of the EED indicates that there is some amount of both continuous acceleration and nonlocal heating of electrons downstream. Along the F3 field line, there is a small amount of heating from position 1 ( $z=27$  cm) to position 2 ( $z=18$  cm), as shown in Fig. 5(c). Once again electrons at position 3 ( $z=9$  cm) have a colder high energy tail due to the larger column density of gas they have traversed and smaller electric fields in the periphery of the reactor. In comparing EEDs, on the three flux lines at a given axial position, the electron population is typically hotter closer to the coil. For example, the high energy tail of the EEDs at position 1 ( $z=27$  cm) increases from F1 to F3, making a transition from being near the center line of symmetry where the electric field is low to near the coil where the electric field is higher. An exception is position 3 ( $z=9$  cm) along F3, where the EED has a lower tail due to the longer path traversed and lower electric fields in this region.

The consequences of noncollisional heating by the propagating axial wave should become more pronounced with decreasing pressure due to the longer mean free paths of electrons. For example, the average mean free paths of electrons along F2 with energy between 5 and 15 eV and electrons above 15 eV are shown in Fig. 6. The mean free path,  $\lambda$ , for electrons in these energy ranges is defined as

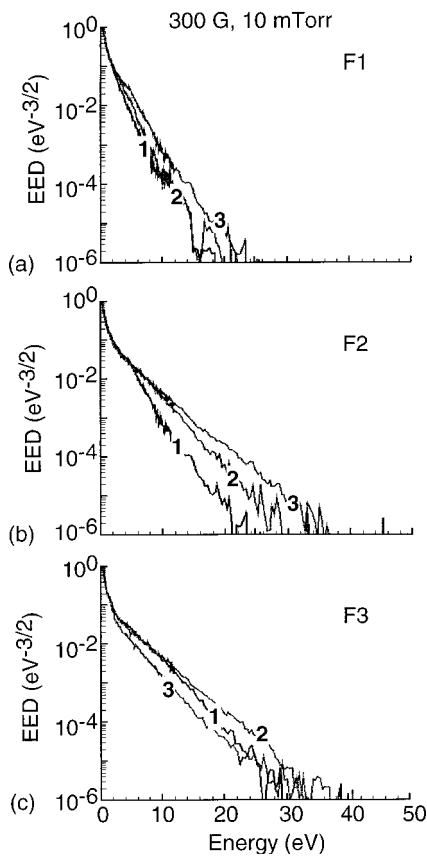


FIG. 5. EEDs along the magnetic flux lines: (a) F1, (b) F2 and (c) F3. EEDs are shown for reference axial positions 1 ( $z=27$  cm), 2 ( $z=18$  cm) and 3 ( $z=9$  cm) for 300 G and 10 mTorr. The tail of the EEDs is raised downstream.

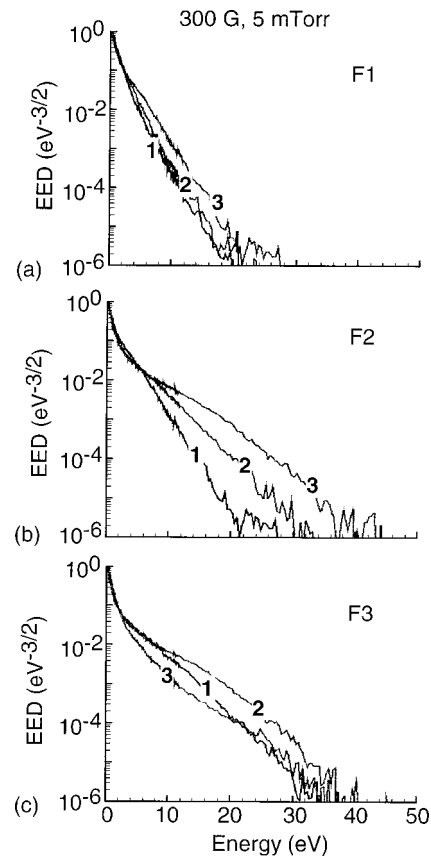


FIG. 7. EEDs along the magnetic flux lines: (a) F1, (b) F2, and (c) F3. EEDs are shown at reference axial positions 1 ( $z=27$  cm), 2 ( $z=18$  cm), and 3 ( $z=9$  cm) for 300 G and 5 mTorr. There is continual lifting of the tail further downstream along F2.

$$\lambda(\bar{r}) = \left( N_g(\bar{r}) \frac{\int_{E_L}^{E_H} \sigma_T(\epsilon) f(\epsilon, \bar{r}) \epsilon^{1/2} d\epsilon}{\int_{E_L}^{E_H} f(\epsilon, \bar{r}) \epsilon^{1/2} d\epsilon} \right)^{-1}, \quad (16)$$

where  $N_g$  is the background gas density,  $\sigma_T$  is the total collision cross section, and  $E_L$  and  $E_H$  bound the energy range

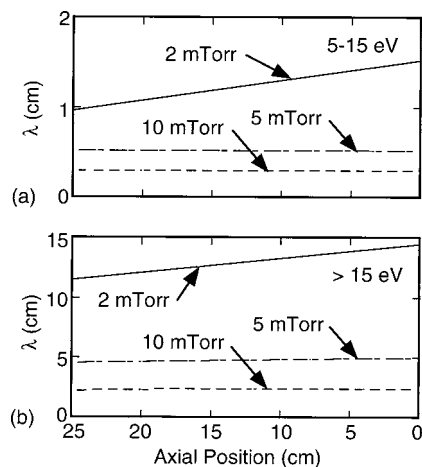


FIG. 6. Mean free path as a function of axial position for 2, 5, and 10 mTorr. (a) For electrons with energy between 5 and 15 eV and (b) for electrons with energy above 15 eV. Low energy electrons have shorter mean free paths and are more collisional.

of interest. Electrons with energy between 5 and 15 eV have mean free paths ranging from 0.5 cm at 10 mTorr to 2 cm at 2 mTorr, as shown in Fig. 6(a) while electrons with energy higher than 15 eV have mean free paths ranging from 2 cm at 10 mTorr to 12 cm at 2 mTorr, as shown in Fig. 6(b). Electrons below 5 eV have mean free paths of the order of 0.01–0.1 cm in the 2–10 mTorr range.

The large mean free path of high energy electrons at low pressure allows substantial noncollisional heating to occur in the propagating electric field. For example, EEDs for 5 and 2 mTorr at 300 G are shown in Fig. 7 and Fig. 8, respectively (the EEDs for 10 mTorr are in Fig. 5). At 5 mTorr, the high energy tail of the EEDs increases with increasing distance from the coil in the axial direction, and decreases with increasing distance from the coil in the radial direction. Both trends are consistent with continual acceleration and noncollisional heating by axial electric fields. At 2 mTorr, these trends become even more pronounced. Along F1, positions 1 and 2 produce a similar EED, while the EED at position 3 has a significantly more pronounced high energy tail, shown in Fig. 8(a). Along F2, a progressive increase in the high energy tail occurs with increasing axial distance from the coil, shown in Fig. 8(b). As previously seen, the high energy tail of the EEDs increases on flux lines closer to the coil. Note that the mean free path at 2 mTorr increases with distance downstream. This trend results from a lifting of the tail of the EED, shifting a larger fraction of electrons to higher

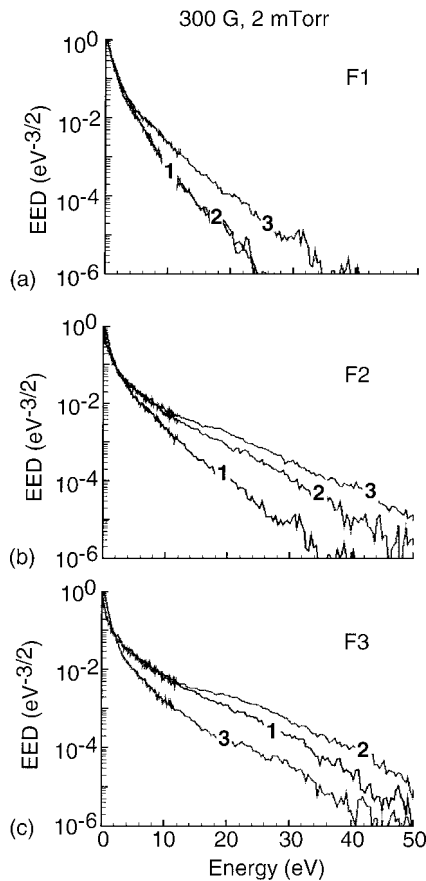


FIG. 8. EEDs along the magnetic flux lines: (a) F1, (b) F2, and (c) F3. EEDs are shown at reference axial positions 1 ( $z=27$  cm), 2 ( $z=18$  cm), and 3 ( $z=9$  cm) for 300 G and 2 mTorr. The longer mean free paths at lower pressure produce more noncollisional heating.

energies where the total scattering cross section is smaller. This allows more efficient acceleration and is akin to a runaway electron effect.

Radially averaged EEDs at 10 mTorr for several magnetic field strengths as a function of axial position are shown in Fig. 9. The EED was averaged over a radius of 10 cm. The arrows indicate the axial position of the rf coils. At 20 G, the EED is most extended (indicating a hot tail) near the coils where most of the power deposition occurs as in conventional ICP systems. At this magnetic field, the axial electric field is not significant, thereby limiting the amount of noncollisional power deposition downstream. Hot electrons thermalize as they diffuse into the downstream region, thereby decreasing the electron EED at 20 eV from  $10^{-4} \text{ eV}^{-3/2}$  near the coils to  $2 \times 10^{-6} \text{ eV}^{-3/2}$  near the substrate. As the magnetic field is increased to 150 G, the magnitude of the axial electric field increases, radial diffusion is decreased and the relative conduction in the axial direction is increased. An increase in axial mobility does not necessarily translate into a monotonically larger high energy tail downstream. At this pressure, there appears to be a local equilibrium between acceleration by the axial electric field and the power absorbed by collisional processes. This results in electrons accelerated by the axial electric field depositing their power locally. As a result hot electrons produced near the coils maintain their energy in the downstream region. For ex-

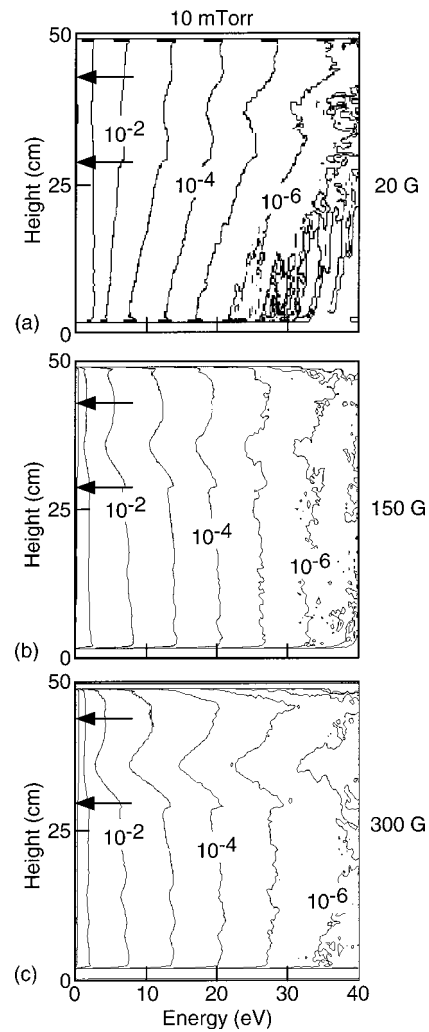


FIG. 9. Radially averaged EED as a function of axial position for 10 mTorr: (a) 20, (b) 150, and (c) 300 G. Near equilibrium may occur between acceleration and collisional damping.

ample, at 300 G, the EED of electrons at 20 eV is nearly the same near the coils and the substrate, as shown in Fig. 9(c). At 10 mTorr, noncollisional heating does not appear to dominate.

As the pressure is reduced, the increase in mean free path and decrease in collisional processes enables continuous acceleration by the axial electric field far into the downstream region. For example, the radially averaged EED at 300 G for 2 and 5 mTorr as a function of axial position is shown in Fig. 10. As the pressure is decreased from 10 [Fig. 9(c)] to 5 and finally to 2 mTorr, the tail of the EED downstream is raised through noncollisional heating. The population of electrons at 30 eV near the substrate increases from  $5 \times 10^{-6} \text{ eV}^{-3/2}$  at 10 mTorr to  $4 \times 10^{-3} \text{ eV}^{-3/2}$  at 2 mTorr.

The ability to deposit power nonlocally through Landau damping depends upon matching the parallel phase velocity of the propagating wave with the thermal velocity of a large fraction of the electron population. The more closely matched these velocities are for a larger fraction of the electron population, the more likely electrons are to be resonantly accelerated. The parallel phase velocity of the electric fields is proportional to the rf frequency. For example, radi-

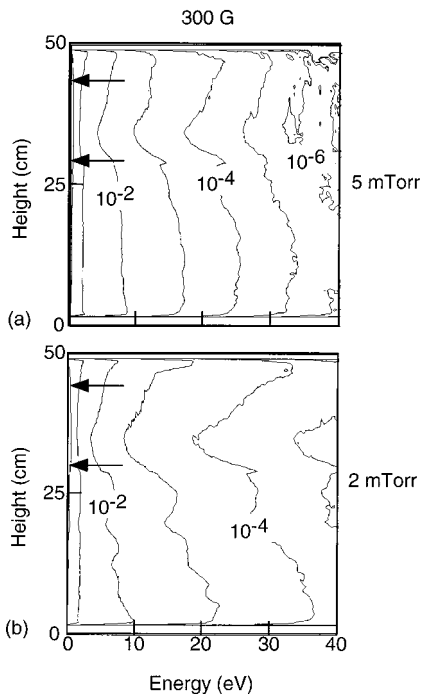


FIG. 10. Radially averaged EED as a function of axial position for 300 G. (a) 5 and (b) 2 mTorr. Significant heating occurs downstream.

ally averaged EEDs at 300 G and 2 mTorr for 27.1 and 1.36 MHz as a function of axial position are shown in Fig. 11. As the rf frequency is decreased from 27.1 to 1.36 MHz, non-collisional heating throughout the reactor becomes more prevalent due to better phase matching with thermal electrons. The population of electrons at 30 eV near the substrate increases from  $10^{-6} \text{ eV}^{-3/2}$  at 27.1 MHz to  $3 \times 10^{-4} \text{ eV}^{-3/2}$  at 1.36 MHz. The proposal is that this increased heating is due to better phase matching.

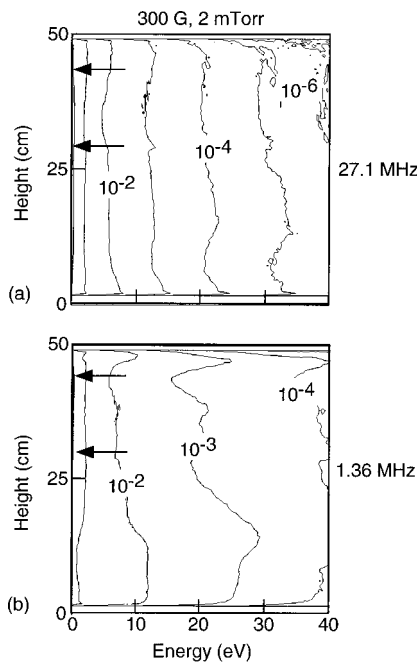


FIG. 11. Radially averaged EED as a function of axial position for 300 G, 2 mTorr. (a) 27.1 and (b) 1.36 MHz.

To determine if the increase in the high energy tail was indeed a result of better phase matching of thermal electrons to the wave phase velocity or simply a skin depth effect, the population of electrons that are capable of being continuously heated through Landau damping was estimated. The electrons which are likely to be continuously accelerated are those having a thermal speed within a factor of  $\lambda_z/2L$  of the phase velocity, where  $\lambda_z$  is the axial wavelength of the electric field and  $L$  is the length of the reactor. This criterion limits electrons to at worst a  $\pi/2$  phase slip relative to the wave. This fraction,  $\beta$ , is obtained from the EED at each location in reactor from,

$$\beta(\bar{r}) = \int_{v_\phi[1-(\lambda_z/2L)]}^{v_\phi} f(v, \bar{r}) dv, \quad (17)$$

where  $v_\phi$  is the phase velocity of the axial wave. The axial wavelength is obtained through a numerical fit of the propagating phase fronts. As described in Ref. 33, we also found that

$$\lambda_z \text{ (cm)} = \frac{7.6 \times 10^6}{R \text{ (cm)}} \left( \frac{B \text{ (G)}}{n_e \text{ (cm}^{-3}\text{)}} \right)^{0.63}. \quad (18)$$

The parallel phase velocity,  $v_\phi$ , is defined as the product of the frequency and the axial wavelength.

The fraction of electrons in phase with the electromagnetic field for rf frequencies of 1.36, 13.56 and 27.1 MHz is shown in Fig. 12. At 27.1 MHz, the fraction of the electrons in phase with the field peaks at about 15% near the substrate. In general, electrons are too cool (slow) to phase match with the electric field. At 1.36 MHz, the fraction of electrons capable of phase matching can reach up to 35% near the coils so electrons are most efficiently heated in the bell jar region. This heating then extends significantly downstream. Due to the large mean free path of electrons above 15 eV noncollisional power absorbed in the bell jar can be deposited downstream. Electron temperatures for these rf frequencies are shown in Fig. 13. For frequencies varying from 1.36 to 27.1 MHz, the mean free path for electrons above 15 eV is between 10 and 20 cm. At 27.1 MHz, electrons are not well matched with the propagating wave and noncollisional absorption is minimal. Electron temperatures peak near the coils where power deposition is limited by the skin depth, as shown in Fig. 13(a). There is a small increase in the electron temperature near the bottom of the chamber. In this region electrons begin to be better phase matched to the propagating wave, as shown in Fig. 12(a). At 1.36 MHz, electrons are well matched in the bell jar and substantial noncollisional acceleration occurs. This acceleration enables phase matching downstream. The energy gained from the propagating wave is deposited further downstream due to the long mean free paths.

Several investigators have measured abrupt increases in plasma density as the static magnetic field is increased.<sup>5,7,14,37</sup> For example, Boswell and Chen made measurements of ion density in a 10 cm diam glass tube using a double Langmuir probe oriented along the magnetic field.<sup>5</sup> The observed increase in the ion density with magnetic field was attributed to narrowing of the plasma column and to an

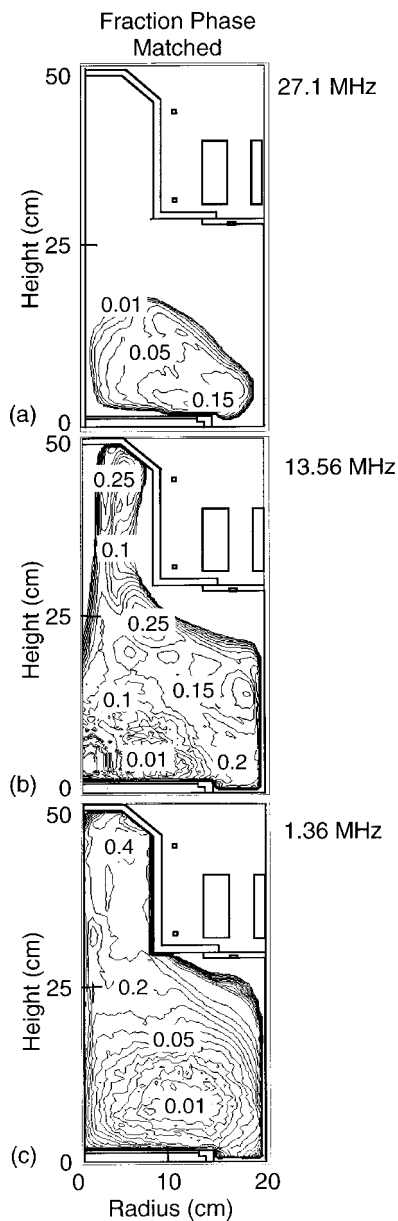


FIG. 12. Fraction of electrons that are in phase with the rf electric field for 300 G and 2 mTorr. (a) 27.1, (b) 13.56, and (c) 1.36 MHz. Electrons are better phase matched at the lower frequency where up to 40% of the population can be in phase with the rf field.

increase in the ionization efficiency by improved coupling of the electrons to the helicon wave. The magnitudes of the jumps in plasma density often measured in these experiments are factors of 2–10 while the total power deposition is constant. If the change in density is attributed solely to an increase in efficiency, then the change in power dissipation mechanisms from nonionizing to ionizing must have similarly increased by factors of 2–10. In rare gases such as Ar it is difficult to find such mechanisms. As has been observed in many inductively coupled systems operating in an *H* mode, the total electron population (density integrated over the volume) largely depends only on input power and so should remain somewhat constant with increasing magnetic field. Small increases in the total plasma density with increasing magnetic fields can be attributed to a decrease in perpendicu-

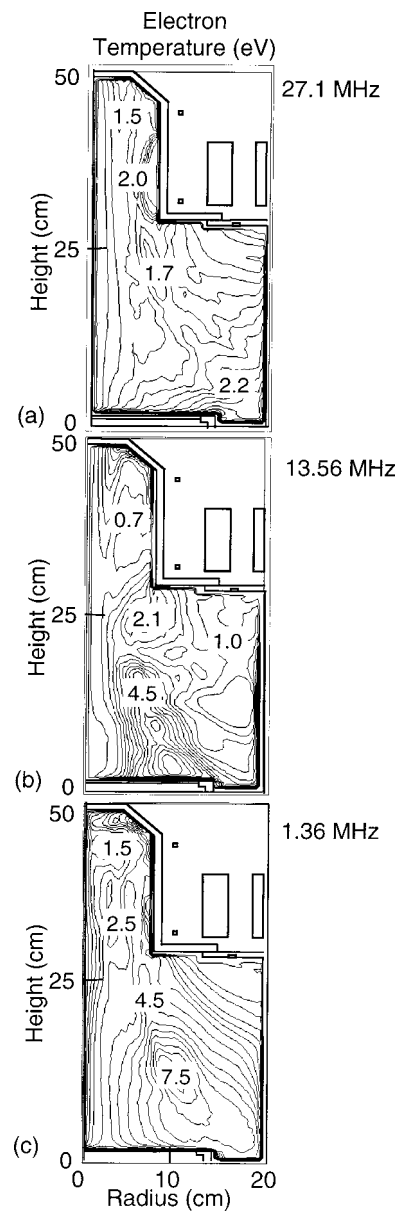


FIG. 13. Electron temperature for 300 G, 2 mTorr. (a) 27.1, (b) 13.56, and (c) 1.36 MHz. At 27 MHz, the electron population is not well phase matched with the rf field and most of the heating is due to collision processes. At 1.36 MHz, electrons are better matched to the rf field. Their long mean free paths allows substantial energy to be absorbed noncollisionally and be deposited downstream.

lar diffusional losses, but not necessarily with a change in ionization mechanism.

It is important to note that most experimental measurements in which plasma density jumps are observed were taken at a single point in the reactor as the magnetic field was varied. The “jumps” may in fact be a result of changes in the distribution of the plasma in the vessel due to changes in the modal electromagnetic wave patterns that in turn determine the location of the power deposition. For example, it was previously shown that as the magnetic field is increased axial propagation of the electromagnetic wave dominates and significant power can be deposited downstream.<sup>33</sup> The peak in the electron density shifts from being near the coils to being located in the downstream chamber. If monitored at a

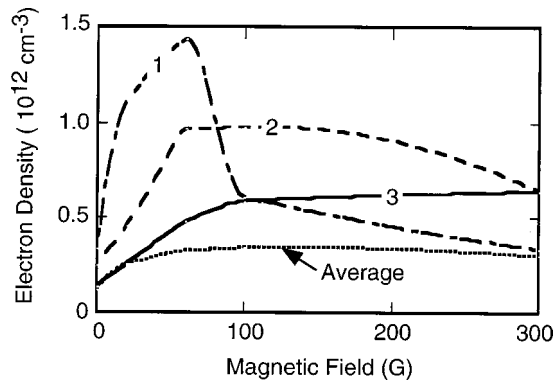


FIG. 14. Electron density as a function of static magnetic field at reference axial positions 1 ( $z=27$  cm), 2 ( $z=18$  cm), and 3 ( $z=9$  cm) along F2 for Ar at 10 mTorr for constant power deposition.

single point, this shift in the plasma density gives the appearance of a large increase in the ionization while the total inventory of electrons does not significantly change.

To demonstrate this effect the electron densities on F2 at positions 1, 2, and 3 are shown in Fig. 14 for Ar at 10 mTorr as a function of magnetic field while keeping the total power deposition constant. The average electron density (total electron inventory divided by the volume of the chamber) is also shown. At 50 G, the electron density at position 1 peaks at  $1.45 \times 10^{12} \text{ cm}^{-3}$ , while at position 3 the electron density is only  $4.5 \times 10^{11} \text{ cm}^{-3}$ . As the magnetic field is increased, the peak plasma density shifts downstream. At 300 G, the electron density at position 1 is  $3.0 \times 10^{11} \text{ cm}^{-3}$ , while at position 3 it is  $6.5 \times 10^{11} \text{ cm}^{-3}$ . While these shifts are occurring, the average density is nearly constant at  $3.0 \times 10^{11} \text{ cm}^{-3}$  from 25 to 300 G. A small increase in average density from 0 to 25 G is likely due to confinement.

#### IV. EFFECTS OF THE ELECTROSTATIC TERM ON PROPAGATION AND HEATING

In order to resolve the TG mode, the divergence term in Eq. (1) was incorporated into the solution for the electromagnetic fields, as described in Sec. II. The azimuthal, radial, and axial electric fields and power deposition are shown in Fig. 15 for 20 G and 2 mTorr. At this low value of the static magnetic field, the electrostatic term significantly affects the propagation and structure of the electromagnetic fields. The azimuthal electric field peaks near the coils and penetrates further into the chamber than in the absence of the electrostatic term. The radial and axial components also show an increased skin depth, however standing wave structures are not as evident. Both  $E_\theta$  and  $E_r$  have maxima near the center of the chamber. The structure in the radial and axial electric fields outside of the bell jar region also changes. This is due to new sources of the electric field which are generated in the bell jar and subsequently propagate away from the sources. Electromagnetic propagation is enhanced in the axial direction, but falls off rapidly at about  $z \approx 12$  cm. At this location the propagating wave encounters an electron cyclotron resonance (ECR) zone where substantial power absorption occurs.<sup>38</sup> At 13.56 MHz, ECR occurs at 4.8 G. For this magnetic field configuration, the 5 G surface lies between  $z$

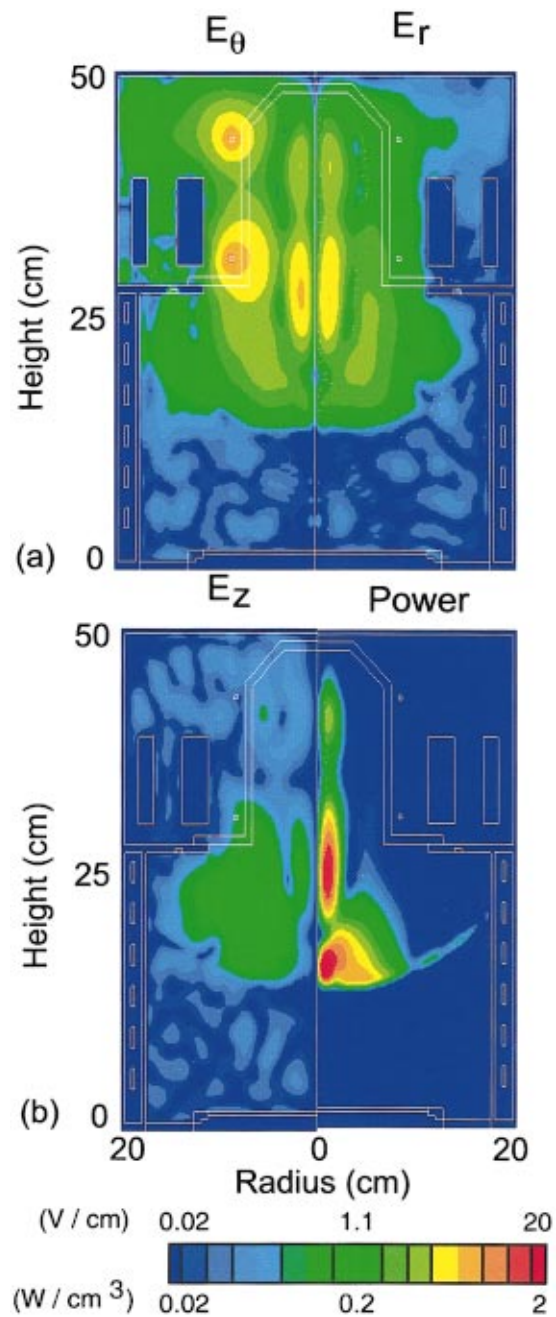


FIG. 15. (Color) Plasma properties obtained when including the electrostatic term in Maxwell's equations for Ar, 20 G, 2 mTorr, and 1 kW power deposition. (a) Azimuthal and radial electric field amplitude and (b) axial electric field amplitude and power deposition. At this low static magnetic field the TG mode enhances the propagation of the wave into the core of the plasma. Propagation continues until the ECR region which is indicated by the local maximum in the power deposition at around  $z=15$  cm.

$=12$  cm on axis and  $z=20$  cm near the chamber wall. Although power deposition peaks near the location of peak electric fields upstream, significant power deposition also occurs in the ECR zone. This ECR heating was not observed at 20 G in the absence of the electrostatic term because the electromagnetic field was largely absorbed upstream and there was less propagation of the electric field downstream to encounter the ECR surface.

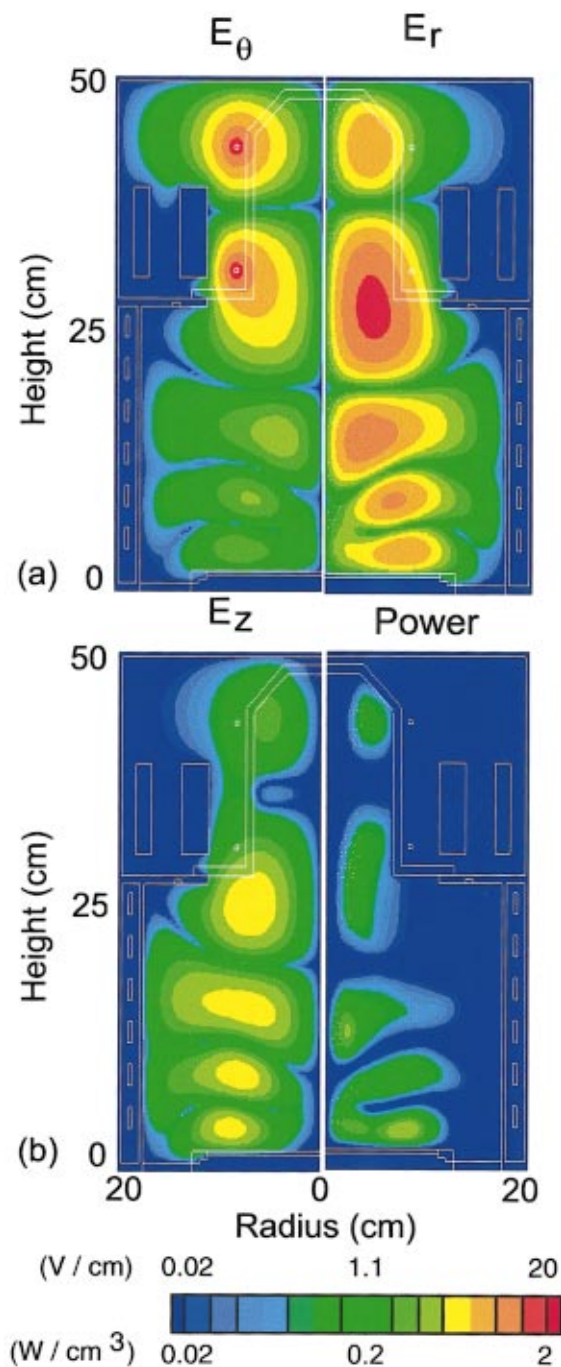


FIG. 16. (Color) Plasma properties when including the electrostatic term in Maxwell's equation for Ar, 300 G, 2 mTorr and 1 kW power deposition. (a) Azimuthal and radial electric field amplitude and (b) axial electric field amplitude and power deposition. At 300 G, the TG mode does not affect the propagation of the wave into the core of the plasma. The propagation resembles the pure helicon mode shown in Fig. 2. There is, however, restructuring of the power deposition near the coils.

The azimuthal, radial and axial electric fields and power deposition with the electrostatic term are shown in Fig. 16 for 300 G. These results are quite similar to those shown in Fig. 2 in the absence of the electrostatic term and indicate that propagation of the electric fields is not significantly altered by the TG mode at higher static magnetic fields. Note that, for these magnetic fields, an ECR surface does not oc-

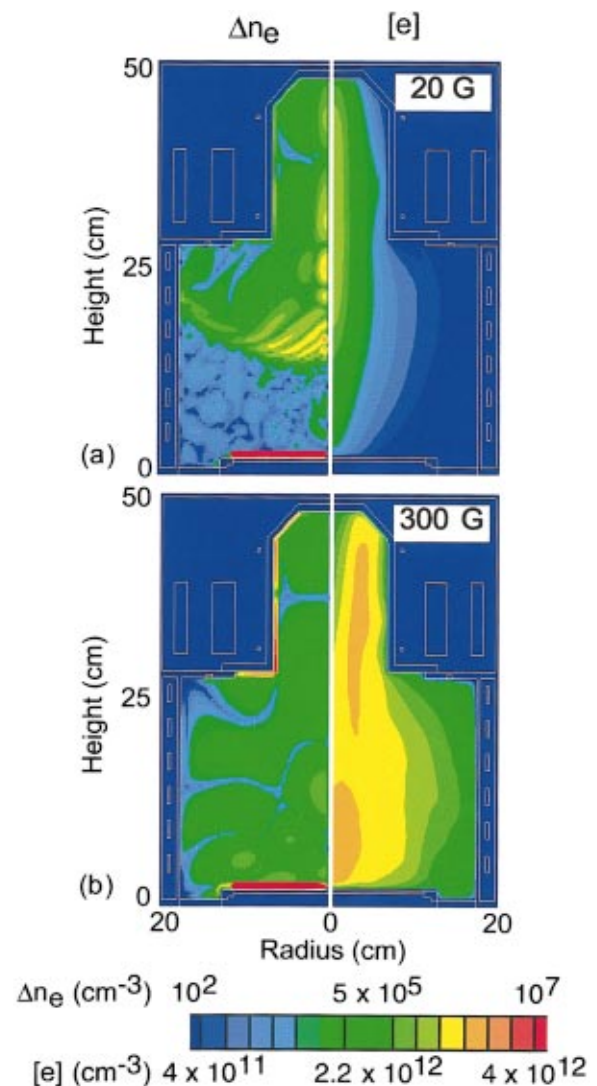


FIG. 17. (Color) Manifestation of the TG mode can be seen through the harmonically driven perturbation in the electron density shown on the left side for (a) 20 and (b) 300 G. The electron density is shown on the right side for (a) 20 and (b) 300 G. At 20 G, the perturbed electron density penetrates into the plasma core, while at 300 G there is significant perturbation only at the bell jar–plasma interface.

cur in the chamber and so does not affect the propagation of the fields.

The manifestation of the electrostatic term can be seen through the harmonically driven perturbation in the electron density shown in the left side of Fig. 17. At 20 G, the perturbed electron density has a small maximum near the bell jar–plasma interface. There is significant propagation into the chamber, with a peak near the axis. Axial propagation occurs until the ECR zone where strong absorption occurs. The electron density at 20 G, shown on the right side of Fig. 17(a), is similar to the pure helicon case shown in Fig. 3(b). The case with the electrostatic term has a lower peak plasma density because a constant power is deposited into a larger volume, thereby also distributing plasma over a somewhat larger volume.

At 300 G, the TG mode is strongly absorbed near the bell jar–plasma interface, as shown on the left side of Fig. 17(b). There is minimal penetration into the chamber at this

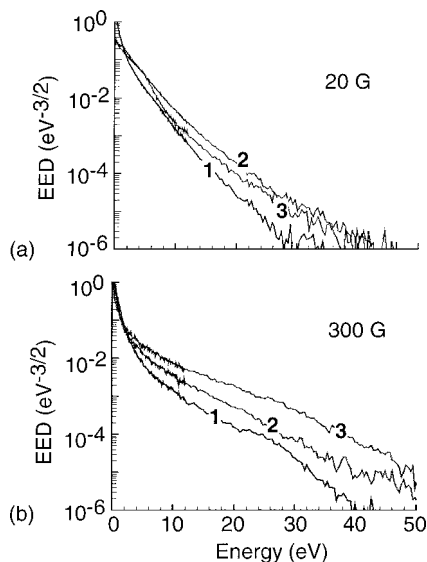


FIG. 18. EEDs along magnetic flux line F2 at reference axial positions 1 ( $z=27$  cm), 2 ( $z=18$  cm), and 3 ( $z=9$  cm) with electrostatic term. (a) 20 G (10 mTorr) and (b) 300 G (2 mTorr).

higher magnetic field. These trends agree with those reported by Shamrai and Taranov who suggested that strongly damped electrostatic waves can reach the plasma core at low magnetic fields, while at high fields they deposit power at the periphery of the plasma column.<sup>27</sup> Since the electromagnetic fields are little affected by the TG mode at 300 G, the electron density profiles are similar to those in the pure helicon case. There is a local maximum in the electron density near the coils and near the substrate where significant power deposition occurs. The peak electron density in the case with the electrostatic term is smaller than for the pure helicon case, but the reactor averaged electron density is higher with the electrostatic term. For the pure helicon case at 300 G and 2 mTorr, the average electron density is  $2.4 \times 10^{11} \text{ cm}^{-3}$ , while with the electrostatic term the average electron density is  $7.7 \times 10^{11} \text{ cm}^{-3}$ .

The EEDs for 20 G at 10 mTorr and 300 G at 2 mTorr with the electrostatic term along F2 are shown in Fig. 18. These EEDs should be compared to Figs. 4 and 8 for results without the electrostatic term. At 20 G, there is a significant raising of the tail of the EED from position 1 ( $z=24$  cm) to position 2 ( $z=16$  cm), indicating some additional downstream heating, perhaps due to the nearby ECR zone, which was not observed in the pure helicon case. Past the ECR zone, at position 3 ( $z=8$  cm), the electron population begins to cool and there is a decrease in the tail of the EED. At 300 G, the tails of the EEDs progressively increase further away from the coil. Including the electrostatic term produces only a small increase in the tail of the EED in comparison with the pure helicon case shown in Fig. 4.

Radially averaged EEDs for 20 G at 10 mTorr and 300 G at 2 mTorr as a function of axial position are shown in Fig. 19. These radially averaged EEDs should be compared to Figs. 9(a) and 10(b) for results without the electrostatic term. Compared to the pure helicon case at 20 G [Fig. 9(a)] there is an increase in the EED population near the coils at 20 eV from  $7 \times 10^{-5}$  to  $5 \times 10^{-4} \text{ eV}^{-3/2}$ , as shown in Fig. 19(a). In

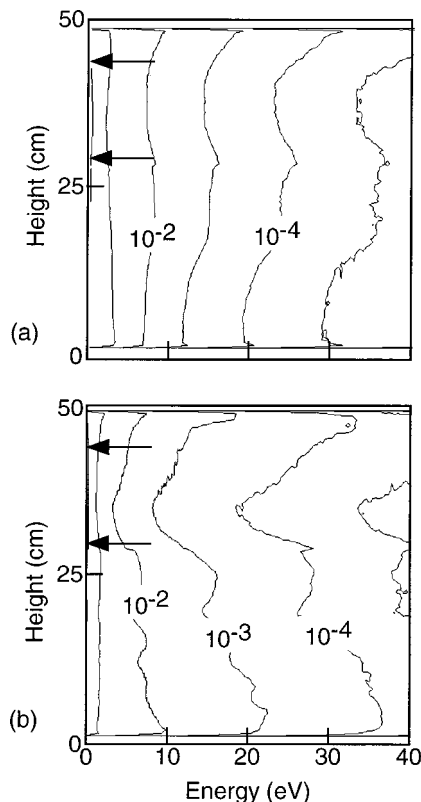


FIG. 19. Radially averaged EED with the electrostatic term as a function of axial position for (a) 20 G (10 mTorr) and (b) 300 G (2 mTorr).

contrast, for 300 G the radially averaged EED with the electrostatic term, shown in Fig. 19(b), is nearly the same as in the pure helicon case, shown in Fig. 11(c). These results again indicate that the TG mode plays a more dominant role in the power deposition at lower magnetic fields. The effect of the TG mode is to restructure the power deposition profile, especially near the coils. However, the propagation of the helicon component is little affected, particularly at large magnetic fields where the TG mode is damped.

### V. CONCLUDING REMARKS

Using a tensor conductivity in the solution of Maxwell's equations, 3D components of the inductively coupled electric field were computed from an  $m=0$  antenna and 2D applied magnetic fields. These fields were used in a Monte Carlo simulation to generate EEDs, transport coefficients and electron impact source functions. In the absence of the electrostatic term, electric field propagation progressively follows magnetic flux lines and significant power can be deposited downstream. When the propagating wave encounters a boundary, such as the substrate, a standing wave pattern forms in the axial direction. The power deposition profiles reflect electromagnetic profiles in the reactor.

The tail of the EEDs were found to increase in magnitude in the downstream chamber for  $B > 150$  G and  $P < 5$  mTorr, indicating some amount of electron trapping and wave heating. This heating results from noncollisional acceleration by the axial electric field for electrons which have long mean free paths in the tail of the EED while low energy

electrons are still somewhat collisional. The mean free path for electrons above 15 eV is between 10 and 20 cm at 2 mTorr. The increase in the high energy tail of the EED is a result of better phase matching of thermal electrons to the phase velocity of the wave. Electrons whose speeds are close to the phase velocity are efficiently heated and subsequently deposit their power downstream through collisions with the background gas. These results indicate that the helicon component of the wave produces significant nonlocal heating.

The TG mode was resolved by including the electrostatic term in the solution of the wave equation. The electrostatic component in the wave equation was approximated by a harmonically driven perturbation of the electron density. The results indicate that strongly damped electrostatic waves can reach the plasma core at low magnetic fields (<20 G), while at high magnetic fields (>150 G) the electrostatic waves deposit power primarily at the periphery of the plasma column. These results indicate that the TG mode plays a more important role in the power deposition mechanisms at lower magnetic fields by restructuring the power deposition profile. The propagation of the helicon component is little affected, particularly at large magnetic fields where the TG mode is damped.

## ACKNOWLEDGMENTS

The authors would like to thank Professor Frank Chen, Professor Rod Boswell, and Professor John Scharer for their helpful discussions during these investigations. This work was supported by the Semiconductor Research Corp., DARPA/AFOSR, National Science Foundation (CTS 99-74962) and Applied Materials.

<sup>1</sup>J. Perry and R. W. Boswell, *Appl. Phys. Lett.* **55**, 148 (1989).

<sup>2</sup>G. Perry, D. Vender, and R. W. Boswell, *J. Vac. Sci. Technol. B* **9**, 310 (1991).

<sup>3</sup>N. Jiwari, H. Iwasawa, A. Narai, H. Sakaue, H. Shindo, T. Shoji, and Y. Horike, *Jpn. J. Appl. Phys., Part 1* **32**, 3019 (1993).

<sup>4</sup>J. E. Stevens, M. J. Sowa, and J. L. Cecchi, *J. Vac. Sci. Technol. A* **13**, 2476 (1995).

<sup>5</sup>R. W. Boswell and F. F. Chen, *IEEE Trans. Plasma Sci.* **25**, 1229 (1997).

<sup>6</sup>G. R. Tynan *et al.*, *J. Vac. Sci. Technol. A* **15**, 2885 (1997).

<sup>7</sup>F. Chen, X. Jiang, and J. Evans, *J. Vac. Sci. Technol. A* **18**, 2108 (2000).

<sup>8</sup>F. F. Chen, *J. Vac. Sci. Technol. A* **10**, 1389 (1991).

<sup>9</sup>F. F. Chen and R. W. Boswell, *IEEE Trans. Plasma Sci.* **25**, 1245 (1997).

<sup>10</sup>S. S. Kim, C. S. Chang, N. S. Yoon, and K-W. Whang, *Phys. Plasmas* **6**, 2926 (1999).

<sup>11</sup>K. N. Ostrikov, S. Xu, and M. Y. Yu, *J. Appl. Phys.* **88**, 2268 (2000).

<sup>12</sup>D. G. Milak and F. F. Chen, *Plasma Sources Sci. Technol.* **7**, 61 (1998).

<sup>13</sup>S. Yun, K. Taylor, and G. R. Tynan, *Phys. Plasmas* **7**, 3448 (2000).

<sup>14</sup>C. Carter and J. Khachan, *Plasma Sources Sci. Technol.* **8**, 432 (1999).

<sup>15</sup>G. Borg and I. Kamenski, *Phys. Plasmas* **4**, 529 (1997).

<sup>16</sup>F. F. Chen, *Plasma Phys. Controlled Fusion* **33**, 339 (1991).

<sup>17</sup>H. Gui and J. E. Scharer, *Proceedings of the IEEE International Conference on Plasma Science*, 1999, p. 141.

<sup>18</sup>A. Degeling, J. E. Scharer, and R. W. Boswell, *Proceedings of the IEEE International Conference on Plasma Science*, 2000, p. 226.

<sup>19</sup>A. Degeling and R. Boswell, *Phys. Plasmas* **4**, 2748 (1997).

<sup>20</sup>A. Molvik, T. Rognlien, J. Byers, R. Cohen, A. Ellingboe, E. Hooper, H. McLean, B. Stallard, and P. Vitello, *J. Vac. Sci. Technol. A* **14**, 984 (1996).

<sup>21</sup>F. F. Chen and D. D. Blackwell, *Phys. Rev. Lett.* **82**, 2677 (1999).

<sup>22</sup>A. Ellingboe, R. Boswell, J. Booth, and N. Sadeghi, *Phys. Plasmas* **2**, 1807 (1995).

<sup>23</sup>A. Degeling, C. Jung, R. Boswell, and A. Ellingboe, *Phys. Plasmas* **3**, 2788 (1996).

<sup>24</sup>J. G. Kwak, *Phys. Plasmas* **4**, 1463 (1997).

<sup>25</sup>W. Trivelpiece and R. W. Gould, *J. Appl. Phys.* **30**, 1784 (1959).

<sup>26</sup>F. F. Chen and D. Arnush, *Phys. Plasmas* **4**, 3411 (1997).

<sup>27</sup>K. P. Shamrai and V. B. Taranov, *Plasma Sources Sci. Technol.* **5**, 474 (1996).

<sup>28</sup>G. G. Borg and R. W. Boswell, *Phys. Plasmas* **5**, 564 (1998).

<sup>29</sup>Y. Mouzouris and J. Scharer, *Phys. Plasmas* **5**, 4253 (1998).

<sup>30</sup>D. Arnush, *Phys. Plasmas* **4**, 2748 (1997).

<sup>31</sup>M. J. Grapperhaus and M. J. Kushner, *J. Appl. Phys.* **81**, 569 (1997).

<sup>32</sup>S. Rauf and M. J. Kushner, *J. Appl. Phys.* **81**, 5966 (1997).

<sup>33</sup>R. Kinder and M. Kushner, *J. Vac. Sci. Technol. A* **19**, 76 (2001).

<sup>34</sup>W. H. Press, B. P. Flannery, S. A. Teukolsky, and W. T. Vetterling, *Numerical Recipes: The Art of Scientific Computing* (Cambridge University Press, Cambridge, 1986).

<sup>35</sup>M. J. Grapperhaus, Z. Krivokapic, and M. J. Kushner, *J. Appl. Phys.* **83**, 35 (1998).

<sup>36</sup>P. L. G. Ventzek, M. Grapperhaus, and M. J. Kushner, *J. Vac. Sci. Technol. B* **12**, 3118 (1994).

<sup>37</sup>T. Kikuchi, K. Ohnishi, Y. Yasaka, K. Tachibana, and T. Itoh, *Jpn. J. Appl. Phys., Part 1* **38**, 4351 (1999).

<sup>38</sup>R. Kinder and M. Kushner, *J. Vac. Sci. Technol. A* **17**, 2421 (1999).